Eur. Phys. J. C (2024) 84:828
https://doi.org/10.1140/epjc/s10052-024-13202-w

THE EUROPEAN PHYSICAL JOURNAL C

Regular Article - Theoretical Physics

Extreme mass-ratio inspiral around the horizonless massive object

Tieguang Zi[1,a], **Liangliang Ren**[2,b], **Jun Cheng**[3,4,c]

[1] School of Physics and Optoelectronics, South China University of Technology, Guangzhou 510641, People's Republic of China
[2] School Electrical and Electronic Engineering, Anhui Science and Technology University, Bengbu 233030, Anhui, China
[3] College of Mathematics and Physics, Hunan University of Arts and Science, Changde 415000, People's Republic of China
[4] Hunan Province Key Laboratory of Photoelectric Information Integration and Optical Manufacturing Technology, Changde 415000, People's Republic of China

Received: 29 May 2024 / Accepted: 5 August 2024

Abstract In this paper, we calculated the extreme mass-ratio inspiral (EMRI) waveform radiated from a binary composed of a massive horizonless object (MHO) and a compact object (CO), where CO is spiraling on a circular equatorial orbit around the MHO. Due to the absent of horizon, there exist the ingoing and outgoing waves near the reflective surface of MHO, which have significantly influence on the evolution of orbital parameters. We observe that there indeed exist the differences of EMRI trajectories between the massive Kerr black hole and MHO cases. By calculating the mismatch of gravitational wave (GW) waveforms from massive black hole (MBH) and MHO, our result indicates that the space-borne gravitational wave detector could distinguish the modified effect of reflectivities from the BH case, which allows to put an upper constraint on the reflectivity $\mathcal{R}$ of MHO, at the level of $\mathcal{R} \gtrsim 10^{-4}$.

Abbreviations

EMRI	Extreme mass-ratio inspiral
MBH	Massive black hole
MCO	Massive compact object
ECO	Exotic compact object
MECO	Massive exotic compact object
MHO	Massive horizonless object
DWD	Double white dwarf
AK	Analytic kludge
NK	Numerical kludge
AAK	Augmented analytic kludge
CO	Compact object
SNR	Signal-to-noise ratio
PN	Post newtonion
FIM	Fisher information matrix
LSO	Last stable orbit
GW	Gravitational wave
BH	Black Hole
BBH	Binary Black Hole
BNS	Binary Neutron Star
NS	Neutron Star
ISCO	Inner stable circle orbit
SNR	Signal-to-noise ratio
GR	General relativity

1 Introduction

The first detection of gravitational wave (GW) event provides a novel avenue for observing CO, notably high-energy astrophysical phenomena in the universe [1,2]. In the recent years, GW astronomy has broadened our understanding of extreme gravity environments with high precision [3–5]. Thus, researchers have begun to explore the strong gravity regime near the BH horizon and accurately map the detailed spacetime structure [6], whereas, the terrestrial GW detectors are not capable of this task due to the seismic noise. The projected space-borne GW observatories, such as LISA [7], TianQin [8] and Taiji [9], aim to unveil the essence of BH horizon and search the smoking gun of new physics [10]. These future GW detectors are expected to observe more kinds of GW sources, providing valuable opportunities to test gravitational theories at unprecedented level [11,12] and investigate the nature of astrophysics BHs whether is suitably described by no-hair hypothesis or not [13–15].

Various horizonless exotic compact objects (hereafter refer to ECO) have been proposed in the literatures, which

[a] e-mail: zitg@scut.edu.cn (corresponding author)
[b] e-mail: rll@ahstu.edu.cn
[c] e-mail: chengjun@huas.edu.cn

Published online: 19 August 2024

include gravastars [16,17], fuzzballs [18], boson stars [19], firewall [20], wormhole [21] and 2–2 holes [22]. In these scenarios, the horizon of Black Hole (BH) is replaced or modified with a surface with non zero reflectivity, which results in the modification of boundary condition for the gravitational perturbation [23–25]. As a consequence, it could be different in the waveforms emitted from the coalescence of binary BHs and ECOs [26–28]. The possibility of testing the existence of BH horizon at Planck scales have been proposed based on the observation of post-merger gravitational wave echo signal using the more sensitive GW detectors [29]. Along with this idea, Refs. [27,30] have analysed the signal of binary BH mergers to seek for tentative evidence of echoes, and their statistical result reached the 2–3σ confidence level. V. Cardoso *et al*. attempted to search for the evidence of existent of ECOs from the merger events of binary BHs, but fails to distinguish ECOs with same angular momentum barrier as same as BHs [31]. Recently, J. Abedi put an upper constraint on echoes amplitude $A < 0.42$ at 90% confidence level, assuming that all 65 BH events have the evidence of echo signals. They pointed out that the next generation GW detectors have potential to search for the smoking gun of echoes or alternatives of general relativity (GR) [32].

A stellar-mass body with $\mu \sim 1 - 10^2 M_\odot$ is captured by massive compact object (MCO) with $M \sim 10^4 - 10^7 M_\odot$, the binaries could lead to an EMRI with a smaller mass-ratio($\eta \leq 10^{-4}$), where the secondary body spirals into the strong field of MCO. Thus, EMRI waveforms carry invaluable information about the central MCO, for example the mass, spin and reflectance of surface of MHO. This makes EMRI a promising tool for mapping the nature of central object [14,33–35] and exploring potential new physics [10,35]. To carry out these goals, a more accurate waveform template for EMRI with MHO is urgently needed. The EMRI waveform about MHO has been carefully calculated using the BH perturbation theory [36,37], which take into account the several novel effects, such as tidal heating [38–42], modified energy fluxes [43,44], area quantization [45,46], and tidal deformability [41,42]. Recently, Maggio et al. computed GW signal from binary system composed of a Kerr-like horizonless MCO and a stellar-mass CO by solving the Teukolsky equation with a modified boundary condition for the in-going mode, and put the stringent constraint about reflectivity of ECO at the level of $\mathcal{O}(10^{-6})\%$ [43]. Similarly, Sago et al. developed the energy flux formulas in term of the asymptotic coefficients of the in-going and out-going homogeneous solutions of Teukolsky radial equation. They found that the energy flux near the reflective surface shows the oscillating part and the non-oscillating part, the modification is enough significant to be detected by the future GW detector [44]. Since the true feature of reflective surface for the exotic compact object (ECO) is agnostic [10], it is difficult to quantitatively simulate the nature of the surface.

Hence, we adopt the ad hoc scheme that the main nature of surface can be described by defining the transfer function, then evolve the orbital radius adiabatically and calculate the EMRI waveform. Maggio et al. and Sago et al. start to consider the asymptotic behavior of the homogeneous solution near the horizon and at the infinity, then compute the fluxes in the ECO case with the asymptotic coefficients [43,44]. In our paper, from the viewpoint of fluxes produced by the reflective surface, we structure the transfer function describing the feature of compact surface, which is the ratio of the reflective and incidence fluxes near the surface. Our method is essentially different from the means developed by Refs. [43,44], which can capture the main features of the reflective surface in a way. We expect that the method can characterize the role of the reflective surface in the orbital evolution of EMRI.

This paper is organized as follows. In Sect. 2, we present the calculation recipes of EMRI waveform in the spacetime of MHO, which includes the following subsections. First, we introduce the spacetime background in Sect. 2.1. Then, we describe the gravitational perturbation formalisms about MHO in Sect. 2.2. Next, we introduce transfer function in Sect. 2.3, followed by energy flux of horizonless object in Sect. 2.4. In Sect. 2.5 we outline the formalism of waveform and mismatch. Finally, we detail the procedure of waveform generation in Sect. 2.6. We show the result in Sect. 3 and conclusion in Sect. 4. Throughout this paper, the geometric units $G = c = 1$ are utilized.

2 Method

2.1 Background

In this paper, we consider that the exterior geometry of a rotating ECO is described by the Kerr BH with a microscopic corrections at the horizon scale [27,47]. In particular, the spacetime is fully described by the Kerr metric if the condition $r > r_0$ is satisfied, and at the location $r = r_0$, the event horizon is replaced with the reflective surface. The exterior geometry of the ECO with spin a and mass M in Boyer–Lindquist coordinates is given by line element

$$ds^2 = \frac{\Sigma}{\Delta}dr^2 + \Sigma d\theta^2 + \frac{\sin^2\theta}{\Sigma}\left[(r^2+a^2)d\phi - adt\right]^2 - \frac{\Delta}{\Sigma}\left[a\sin^2\theta d\phi - dt\right]^2, \quad (1)$$

where $\Sigma = r^2 + a\cos^2\theta$ and $\Delta = r^2 - 2Mr + a^2 = (r-r_+)(r-r_+)$, with $r_\pm = M \pm \sqrt{M^2 - a^2}$. The root r_+ is regarded as the location of the would-be horizon for the horizonless ECOs. In this paper, the effective reflective surface is introduced in the neighbourhood of would-be horizon, which

locates at r_0,

$$r_0 = r_+(1+\delta). \tag{2}$$

Given that the microscopic corrections, the parameter δ should be met the following condition $0 < \delta \ll 1$. The parameter δ is a tiny quantity or the Planck length l_P [25,48], it also is far less than the gravitational radius of massive ECOs, and the case $\delta \to 0$ denotes to the BH limit. The modifications of the metric are suppressed by the series of $l_P/r_0 \ll 1$, where r_0 is the radius of the central object [49].

In fact, in the frame of GR, the deviation from the spacetime structure of Kerr BH would be decay to zero fast, and the deviation effects within the modified gravities are limited also near the gravitational radius r_0 [50]. Therefore, it is feasible that the exterior spacetime of a spinning ECO can be described by the Kerr metric with a reflective surface.

2.2 Gravitational perturbation formalisms

In this subsection, we informally introduce the formula of Kerr spacetime perturbation. The gravitational linear perturbation of Kerr black hole is described by the Teukolsky equation [51–53], where Newman–Penrose scalar curvature Ψ_4 encompasses the full information of gravitational perturbation. At infinity $r \to \infty$, two polarization modes h_+ and $h_\times$ of GW can be extracted from the Newman–Penrose scalar curvature Ψ_4

$$\Psi_4(r\to\infty) = \frac{1}{2}\frac{\partial^2}{\partial t^2}(h_+ - ih_\times), \tag{3}$$

and it is separated into radial function $R_{\ell m\omega}$ and spin-weighted spheroidal harmonic ${}_{-2}S_{\ell m\omega}$

$$\Psi_4 = \rho^4 \sum_l \sum_{m=\ell}^{m=-\ell} \int_{-\infty}^{\infty} R_{\ell m\omega} S_{\ell m\omega} e^{-i\omega t + im\phi}, \tag{4}$$

where $\rho = (r - ia\cos\theta)^{-1}$. In order to solve spheroidal harmonic ${}_{-2}S_{\ell m\omega}$ numerically, we adopt the Black Hole Perturbation Toolkit's [54] Mathematica package SpinWeightedSpheroidalHarmonics. The Teukolsky master equation about radial function $R_{\ell m\omega}$ can be read off as the following

$$\Delta^2 \frac{d}{dr}\left(\frac{1}{\Delta}\frac{dR_{\ell m\omega}}{dr}\right) - V(r)R_{\ell m\omega} = \mathcal{T}_{\ell m\omega}, \tag{5}$$

and

$$V(r) = -\frac{K^2 + 4i(r-M)K}{\Delta} + 8i\omega r + \lambda + a^2\omega^2 - 2am\omega, \tag{6}$$

where $V(r)$ is the effective potential function, $K(r) = (r^2 + a^2)\omega - am$, λ is the eigenvalue of spheroidal harmonic. The source term $\mathcal{T}_{\ell m\omega}$ is showed in appendix B.

Teukolsky radial equation (5) has two sets of independent homogeneous solutions, $R^{\rm out}_{\ell m\omega}$ and $R^{\rm in}_{\ell m\omega}$, with the following asymptotic behaviors

$$R^{\rm in}_{\ell m\omega} \sim \begin{cases} B^{\rm trans}_{\ell m\omega}\Delta^2 e^{-ikr_*} & \text{as } r_* \to -\infty \\ r^3 B^{\rm ref}_{\ell m\omega} e^{i\omega r_*} + r^{-1} B^{\rm inc}_{\ell m\omega} e^{-i\omega r_*} & \text{as } r_* \to +\infty \end{cases}, \tag{7}$$

$$R^{\rm out}_{\ell m\omega} \sim \begin{cases} C^{\rm out}_{\ell m\omega} e^{ikr_*} + \Delta^2 C^{\rm ref}_{\ell m\omega} e^{-ikr_*} & \text{as } r_* \to -\infty \\ r^3 C^{\rm trans}_{\ell m\omega} e^{i\omega r_*} & \text{as } r_* \to +\infty \end{cases}, \tag{8}$$

where $\kappa = \omega - am/(2r_+)$, and r_* is the tortoise coordinate,

$$r_*(r) = r + \frac{2Mr_+}{r_+ - r_-}\ln\frac{r - r_+}{2M} - \frac{2Mr_-}{r_+ - r_-}\ln\frac{r - r_-}{2M} \tag{9}$$

which is obtained by $dr_*/dr = (r^2 + a^2)/\Delta$.

Since the asymptotic value of homogeneous radial Teukolsky equation includes the term r^3, the solution inevitably diverges at infinity. To circumvent such problem, Sasaki and Nakamura devised a suitable equation with a short ranged potential, which is referred to as the SN equation [55,56]. Then the asymptotic behaviors become

$$X^{\rm in}_{\ell m\omega} \sim \begin{cases} {}_{\rm SN}B^{\rm trans}_{\ell m\omega} e^{-i\kappa\omega}, & r \to r_+ \\ {}_{\rm SN}B^{\rm ref}_{\ell m\omega} e^{-i\omega r_*} + {}_{\rm SN}B^{\rm inc}_{\ell m\omega} e^{i\omega r_*}, & r \to \infty \end{cases} \tag{10}$$

$$X^{\rm out}_{\ell m\omega} \sim \begin{cases} {}_{\rm SN}C^{\rm ref}_{\ell m\omega} e^{-i\kappa r_*} + {}_{\rm SN}C^{\rm inc}_{\ell m\omega} e^{i\kappa r_*}, & r \to r_+ \\ {}_{\rm SN}C^{\rm trans}_{\ell m\omega} e^{i\omega r_*}, & r \to \infty \end{cases} \tag{11}$$

where ${}_{\rm SN}(C, B)^{\rm trans,ref,inc}_{\ell m\omega}$ and $(C, B)^{\rm trans,ref,inc}_{\ell m\omega}$ can be transformed each other, the factors between them is placed in Append A.

2.3 Transfer function

The general solution $R_{\ell m\omega}$ of the radial Teukolsky equation behaves as near horizon $r \to r_+$,

$$R_{\ell m\omega} \sim A^{\rm in}\Delta^2 e^{-ikr_*} + A^{\rm out}e^{ikr_*}, \tag{12}$$

and it can transfer to the solution of SN equation in the equivalent form

$$R_{\ell m\omega} \sim A^{\rm in}_{\rm SN} e^{-ikr_*} + A^{\rm out}_{\rm SN} e^{ikr_*}, \tag{13}$$

the in-going and out-going fluxes near the horizon are [57,58]

$$E^{\rm in}_H = \frac{128\omega k(2Mr_+k)^5(k^2+16\bar{\epsilon})}{|c_{\ell m}|^2}|A^{\rm in}|^2 = \frac{8\omega k}{|c_{\ell m}|^2}|A^{\rm in}_{SN}|^2, \tag{14}$$

$$E^{\rm out}_H = \frac{\omega}{2k(2Mr_+)^3(k^2+\bar{\epsilon}^2)}|A^{\rm out}|^2 = \frac{8\omega k}{b_0^2}|A^{\rm out}_{SN}|^2, \tag{15}$$

where the constant $\bar{\epsilon} = (r_+ - M)/(4Mr_+)$, the full expressions of $|c_{\ell m}|^2$ and b_0 are found in Append A and Append B.

To construct inhomogeneous solution of SN equation for the MHO case, we adopt the method of Refs. [30,48,59] by including the transfer function, where the inhomogeneous

solution for the horizonless spacetime can be combination of ingoing and outgoing modes in Kerr spacetime. The combination equation can be written as

$$X^{\rm ECO}_{\ell m\omega}(r) = X^{\rm in}_{\ell m\omega}(r) + \mathcal{K}_{\ell m\omega} X^{\rm out}_{\ell m\omega}(r), \tag{16}$$

where $\mathcal{K}_{\ell m\omega}$ is transfer function, and the similar expression is found in [59]. In term with Eqs. (14) and (16), one can get the energy flux near the surface of MHO

$$E^{H}_{\rm in} = \frac{8\omega k}{|c_{\ell m}|^2}\left|1 + \mathcal{K}_{\ell m\omega}\frac{{}_{\rm SN}C^{\rm ref}}{{}_{\rm SN}C^{\rm trans}}\right|^2, \tag{17}$$

$$E^{H}_{\rm out} = \frac{8\omega k}{b_0^2}\left|\mathcal{K}_{\ell m\omega}\frac{{}_{\rm SN}C^{\rm inc}}{{}_{\rm SN}C^{\rm trans}}\right|^2, \tag{18}$$

We assume that the reflectivity of MHO is proportion to the ratio of the out-going and in-going fluxes near the reflective surface, then the transfer function $\mathcal{K}_{\ell m\omega}$ is given by

$$\begin{aligned}\mathcal{K}_{\ell m\omega} &= \frac{b_0}{|c_{\ell m}|}\frac{{}_{\rm SN}C^{\rm trans}}{{}_{\rm SN}C^{\rm inc}}\frac{\mathsf{R}}{1-\frac{b_0}{|c_{\ell m}|}\frac{{}_{\rm SN}C^{\rm ref}}{{}_{\rm SN}C^{\rm trans}}\mathsf{R}},\\ &= -\frac{b_0}{|c_{\ell m}|}\frac{c_0 C^{\rm trans}}{4\omega g C^{\rm inc}}\frac{\mathsf{R}}{1-\frac{b_0}{|c_{\ell m}|}\frac{dC^{\rm ref}}{gC^{\rm trans}}\mathsf{R}},\end{aligned} \tag{19}$$

where c_0, d and g is placed in Append A, $\mathsf{R} = \mathcal{R}e^{-2i\kappa x_0}$ is the frequency-dependent reflectivity of MHO, x_0 is location of reflectivity surface and the reflectivity of surface is constant, that is $\mathcal{R} \in (0, 1]$. The reflectivity parameter $\mathcal{R} = 0$ for the horizon of classical BH. If the horizonless massive object is perfect reflector, the parameter $\mathcal{R} = 1$. The formula of transfer function is similar to Eq. (16) of Ref. [59].

2.4 Enengy flux of horizonless object

In the case of MHO, the in-going solution of the Teukolsky function is given by

$$R^{\rm in,ECO}_{\ell m\omega} = R^{\rm in}_{\ell m\omega} + \mathcal{K}_{\ell m\omega} R^{\rm out}_{\ell m\omega} \tag{20}$$

$$= \mathcal{K}_{\ell m\omega} e^{i\kappa r_*} + (\mathcal{Y} + \mathcal{K}_{\ell m\omega}\mathcal{J})\Delta^2 e^{-i\kappa r_*}, \tag{21}$$

where $\mathcal{Y} = B^{\rm trans}/B^{\rm inc}$ and $\mathcal{J} = C^{\rm ref}/C^{\rm out}$, and it has asymptotic behavior

$$R^{\rm in,ECO}_{\ell m\omega} \sim \begin{cases} Z^{\rm H+}_{\ell m\omega} e^{i\kappa r_*} + Z^{\rm H-}_{\ell m\omega} e^{-i\kappa r_*}, & r \to r_+ \\ Z^{\infty}_{\ell m\omega} e^{i\omega r_*}, & r \to \infty \end{cases} \tag{22}$$

where $Z^{\rm H+}_{\ell m\omega}$ and $Z^{\rm H-}_{\ell m\omega}$ is out-going and in-going amplitude respectively near the surface. They can be determined by amplitude $Z^{\rm H}_{\ell m\omega}$ of BH horizon, that is

$$Z^{\rm H+}_{\ell m\omega} = \mathcal{K}_{\ell m\omega} Z^{\rm H}_{\ell m\omega}, \qquad Z^{\rm H-}_{\ell m\omega} = (\mathcal{Y} + \mathcal{K}_{\ell m\omega}\mathcal{J}) Z^{\rm H}_{\ell m\omega}. \tag{23}$$

And $Z^{\infty}_{\ell m\omega}$ and $Z^{\rm H}_{\ell m\omega}$ is amplitude at infinity and near the horizon for the BH spacetime respectively, their full expressions see in Refs. [60,61] and references therein.

In the ECO case, the total energy flux emitted by a point particle on a circular equatorial orbit is given by

$$\dot{E}_{\rm ECO} = \dot{E}^{\rm H}_{\rm ECO} + \dot{E}^{\infty}_{\rm ECO}, \tag{24}$$

where $\dot{E}^{H}_{\rm ECO}$ and $\dot{E}^{\infty}_{\rm ECO}$ is energy flux at horizon and at infinity in the spacetime of MHO, the dot $\dot{}$ denotes the time derivative. The total energy flux in the BH spacetime is

$$\dot{E}_{\rm BH} = \dot{E}^{\rm H}_{\rm BH} + \dot{E}^{\infty}_{\rm BH}, \tag{25}$$

where $\dot{E}^{\rm H}_{\rm BH}$ and $\dot{E}^{\infty}_{\rm BH}$ is energy flux at horizon and at infinity in the Kerr spacetime [60,61]. For the case of ECO, the horizon energy flux $\dot{E}^{H}_{\rm ECO}$ of MHO can be written as

$$\dot{E}^{H}_{\rm ECO} = \dot{E}^{\rm H+}_{\rm ECO} + \dot{E}^{\rm H-}_{\rm ECO}, \tag{26}$$

where the flux expressions of $\dot{E}^{\rm H+}_{\rm ECO}$ and $\dot{E}^{\rm H-}_{\rm ECO}$ are as follows [57,60]

$$\dot{E}^{\rm H-}_{\rm ECO} = \sum_{\ell m}\frac{\alpha_{\ell m}|Z^{\rm H-}_{\ell m\omega}|^2}{4\pi\omega^2} = \sum_{\ell m}\frac{\alpha_{\ell m}|(\mathcal{Y}+\mathcal{K}_{\ell m\omega}\mathcal{J})Z^{\rm H}_{\ell m\omega}|^2}{4\pi\omega^2}, \tag{27}$$

$$\dot{E}^{\rm H+}_{\rm ECO} = \sum_{\ell m}\frac{\alpha_{\ell m}|Z^{\rm H+}_{\ell m\omega}|^2}{4\pi\omega^2} = \sum_{\ell m}\frac{\alpha_{\ell m}|\mathcal{K}_{\ell m\omega}Z^{\rm H}_{\ell m\omega}|^2}{4\pi\omega^2}, \tag{28}$$

where the expression $\alpha_{\ell m}$ is found in Append B. The angular-momentum fluxes at infinity and near the horizon are obtained by the relation

$$\dot{Lz}^{\infty,\rm H} = \frac{\dot{E}^{\infty,\rm H}_{\rm ECO,BH}}{m\Omega_\phi}. \tag{29}$$

where Ω_ϕ is the orbital angular frequency for the equatorial circular orbits. The expression is given by

$$\Omega_\phi = \pm\frac{\sqrt{M}}{(a\sqrt{M} + r^{3/2})}. \tag{30}$$

the plus sign refers to prograde orbit and the minus sign refers to retrograde orbit, which is related with frequency $\omega = m\Omega_\phi$.

The evolution of inspiral trajectory of CO is given by the following differential equation [60,62]:

$$\frac{dr}{dt} = J^c_{E_{r_c}}\dot{E}_{\rm ECO} + J^c_{Lz_{r_c}}\dot{Lz}, \tag{31}$$

where the Jacobian elements are

$$J^c_{E_{r_c}} = \frac{2aM(L_z - aE) - 2a^2Er - 4Er^3}{\mathcal{D}^c(r)}, \tag{32}$$

$$J^c_{Lz_{r_c}} = -\frac{2M(L_z - aE) + 2L_z r}{\mathcal{D}^c(r)} \tag{33}$$

with $\mathcal{D}^c(r) = -[a^2(-E^2) + L_z^2] + 6Mr - 6(1 - E^2)r^2$. Here E and L_z is the circular orbital energy and angular-momentum at a equatorial plane respectively, which is given

by [60]

$$E = \frac{1 - 2v^2 \pm av^3}{\sqrt{1 - 3v^2 \pm 2av^3}}, \tag{34}$$

$$L_z = -rv\frac{1 \pm 2av^3 \pm a^2v^4}{\sqrt{1 - 3v^2 \pm 2av^3}}, \tag{35}$$

with $v = \sqrt{M/r}$, the symbol + and − correspond to prograde and retrograde orbits, respectively.

2.5 Waveform and mismatch

For a standard EMRI system, the time scale of radiation-reaction is much longer than the orbital period, the lose of orbital energy can be caused by the radiation of GW, thus the orbital parameters can be evolved with an adiabatic expansion [63]. The waveform at infinity emitted from EMRI is obtained by following [61]

$$h_+ - ih_\times = -\frac{2}{\sqrt{2\pi}}\frac{\mu}{D}\sum_{\ell,m}\frac{Z^\infty_{\ell m\omega}(t)}{\omega^2}e^{im(\omega r_* - t)} \times {}_{-2}S_{\ell m\omega}(\vartheta, t)e^{im\varphi}, \tag{36}$$

where μ and D is mass of CO and source luminosity distance from the GW detector, respectively, (ϑ, ψ) denote the direction of source in Boyer-Lindquist coordinates, and φ is orbital phase.

With Euler method, one can get the evolution of radius by solving the Eq.(31), and obtain the inspiral trajectory in the spacetime of MHO, then compute the waveform from BH and MHO with Eq. (36). Having two kinds of waveform at hand, one can assess the discrepancy of waveforms quantitatively by calculating the mismatch between two different waveforms $h_1(t)$ and $h_2(t)$. The mismatch $\mathcal{M} \equiv 1 - \mathcal{O}$ is defined by overlap $\mathcal{O}$

$$\mathcal{O}(h_1|h_2) = \frac{\langle h_1|h_2\rangle}{\sqrt{\langle h_1|h_1\rangle\,\langle h_2|h_2\rangle}}, \tag{37}$$

here the inner product $< h_1|h_2 >$ is given by

$$\langle h_1|h_2\rangle = 4\Re\int_0^\infty \frac{\tilde{h}_1\tilde{h}_2^*}{S_n(f)}df, \tag{38}$$

where $S_n(f)$ is the GW detector noise power spectral density for upcoming LISA [7], and the tildes and the star represent Fourier transform and complex conjugation, respectively.

2.6 Waveform generation

We simulate the EMRI dynamics with MHO based on the perturbation theory, assuming that a point-particle motion on the equatorial circular orbits. Concretely, the solutions of the homogeneous Teukolsky equation are computed using Mano-Suzuki-Takasugi method [64–66]. This method allows us to get the analytical boundary conditions, which is well-suited for our purpose.

Before computing the energy flux and waveforms that emitted from MHO, we need to make some preparatory works, which are scheduled as follows:

(1) Source parameter can be divided into two sets: intrinsic and extrinsic parameters.
   - Intrinsic parameters: $(r/M, \mu, M, a, e, \theta_{\rm inc}, \mathcal{R}(\omega), x_0)$. The physical meaning of intrinsic parameters are as follows: the spin a, the location x_0 of reflective surface and reflectivity $\mathcal{R}(\omega)$ of MHO, and the circular orbit radii r at initial moment. We only focus on the equatorial circular orbits, that is the parameter is set as eccentricity $e = 0$ and inclination angle $\theta_{\rm inc} = \pi/2$. The mass of primary and secondary object is set as $M = 10^6 M_\odot$ and $\mu = 10M_\odot$, respectively.
   - Extrinsic parameters: $(\theta_K, \psi_K, \theta_S, \psi_S, D, t_{\rm max})$. Here, the angles (θ_S, ψ_S) are the latitude and azimuth in an ecliptic based coordinate system, the angles (θ_K, ψ_K) denote the direction of the spin of the MHO, with respect to the above coordinate system, and D is the luminosity distance from source to detector, $t_{\rm max}$ is the inspiral time of smaller CO until captured by MCO and the sampling interval takes $\Delta t = 15$ s.

(2) Start the evolution of radial coordinate from $r_0 = 10M$ to $r_{\rm ISCO} + 0.01M$($r_{\rm ISCO}$ refers to the radius of inner stable circle orbit (ISCO)), the trajectory is subjected with the Eq. (31).

(3) For the given radius r, we firstly fix indexes $\ell_{\rm max} = 5$ and $m \in [-\ell, -\ell-1, \ldots, 1, \ldots, \ell-1, \ell]$, then calculate the orbital frequency (30), energy flux for the MHO case (24) and for the MBH case (27). We also calculate the polarization (36) of waveform, finally sum over all modes to compute the waveform. Note that the difference of the energy fluxes for the contiguous modes $\ell_{\rm max}$, $\ell_{\rm max}+1$, $\ell_{\rm max}+2$ is less than the threshold values $\min[10^{-4}, \mathcal{R}]$.

(4) Inject the polarizations Eq. (36) of waveform into the response function of detector using the low-frequency approximation, as described in the relevant literature [67].

3 Results

We present some results regarding the features of GW from the horizonless MHO, and assess the detectability of GW from such sources with future space-borne detector. In Sect. 3.1, we place the energy fluxes, evolution of the orbital radius and waveform in the spacetime of MHO. In Sect. 3.2,

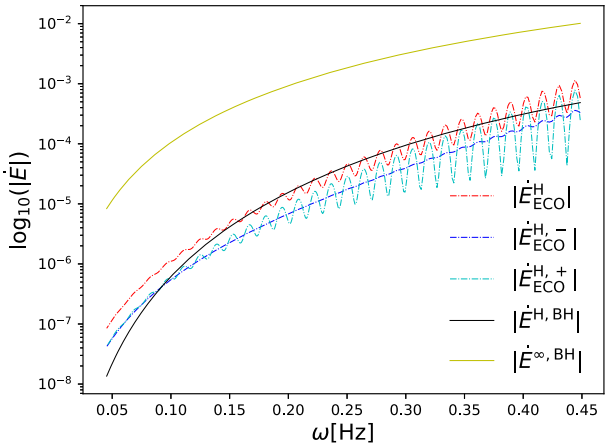

Fig. 1 Energy fluxes from EMRI with MHO and MBH as a function of orbital frequency is plotted, the other parameters is set as $a = 0.9$, $(l, m) = (2, 2)$, the reflectivity $\mathcal{R} = 0.7$ and the mass ratio $\eta = 10^{-5}$

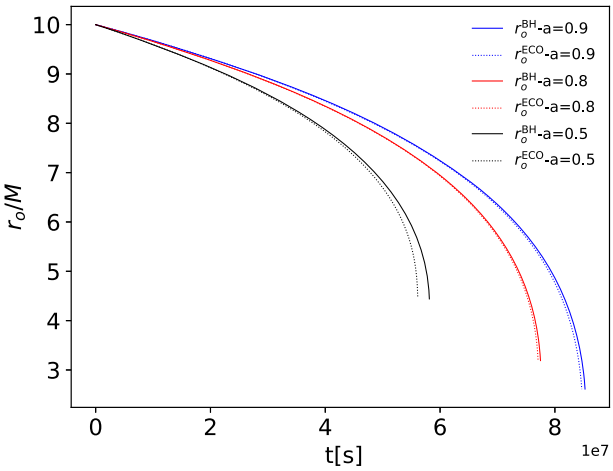

Fig. 2 Evolutions of the orbital radius for EMRI with MBH and MHO are plotted, which include three following cases, $a = 0.5$, $a = 0.8$ and $a = 0.9$. The dynamic evolution of EMRI begins from $10M$ to ISCO

we present the mismatch between two types of waveforms emitted from MBH and MHO.

3.1 Energy fluxes, trajectory and waveform

In this section, we compute the evolution of circular orbital radius under radiation reaction, which include the correction effect of horizonless object for several spinning cases.

The nature of reflective surface for the MHO is described by the transfer function, which is given by Eq. (19). In order to assess the effect of horizonless object on EMRI energy flux, we firstly plot the energy fluxes omitted from EMRI with MHO and MBH using the modified fluxes formulas (28), (28) and (26) in Fig. 1, which include the following case of mode $(\ell, m) = (2, 2)$, mass ratio $\eta = 10^{-5}$ and spin $a = 0.9$ of MCO. Notably, the reflectivity nature of MHO is characterized by the transfer function (19), the value of reflectivity is set as $\mathcal{R} = 0.7$ in Fig. 1. From this figure, one can observe that these oscillations appear in the out-going and in-going energy flux when the orbital frequency gradually increases. Specifically, the out-going energy flux $\dot{E}^{\mathrm{H},+}_{\mathrm{ECO}}$ oscillates more acutely than the in-going one $\dot{E}^{\mathrm{H},-}_{\mathrm{ECO}}$ in the high frequency region. This is duo to the present of the reflected surface and the potential barrier near the MHO, which allows to reprocess emission by a point particle after taking the reflecting boundary into account. As a result, the out-going wave oscillates between the barrier and reflected surface, leading to more violent in the out-going energy flux compared to the in-going one. There exist the similar oscillation phenomenon for the energy flux in Refs. [43,44], energy fluxes near the reflectivity surface is corrected due to the absent of horizon.

We show the trajectories of orbital radius, including different spacetime background, in Fig. 2. The plot shows the orbital radius r_o/M as a function of time t for various spins. The source parameters are assumed that EMRI system composed of MHO (MBH) with mass $10^6 M_\odot$ and spin $a = (0.5, 0.8, 0.9)$, and nospinning CO with mass $10M_\odot$, The reflectivity is set as $\mathcal{R} = 0.8$, and location of surface is $x_0 = -40M$. As shown in the figure, one can see that trajectories of CO for the case of MHO is deviation from the case of BH with the time growing. The difference becomes more obvious for the lower spinning MHO.

Figure 3 depicts the time domain of the polarizations h_+ of waveform radiated from EMRI with MBH and MHO, where the inspiral time of CO in the vicinity of MCO is set to one year. It is found that the early stage of two kind of EMRI waveforms are nearly same, and they gradually shows difference in the waveforms phase with the time is increasing.

3.2 Mismatch

With the energy flux and trajectory at hand, we can compute waveforms from EMRI system with MHO and MBH under radiation reaction, respectively. To evaluate the different kinds of waveforms from MHO and MBH, we place the mismatch as a function of observation time of EMRI for the future space-borne detector, such as LISA.

Figure 4 shows that mismatch as a function of observation time of EMRI for LISA, considering various reflectivities $\mathcal{R}$ and locations x_0 of surface of MHO. Specifically, we plot several cases of EMRI systems with $\mathcal{R} = (10^{-2}, 10^{-3}, 5 \times 10^{-4}, 10^{-4})$, $x_0 = (-60\,M, -150\,M)$, and spin $a = (0.5, 0.9)$. The horizontal dotted line represents the threshold value of mismatch that can be distinguished by LISA, in which threshold value is determined by $\mathcal{M}_{\mathrm{min}} = \mathcal{D}/(2\rho^2)$, ρ as the signal to noise ratio of EMRI signal is set to be 20, and $\mathcal{D} = 9$ is the number of the intrin-

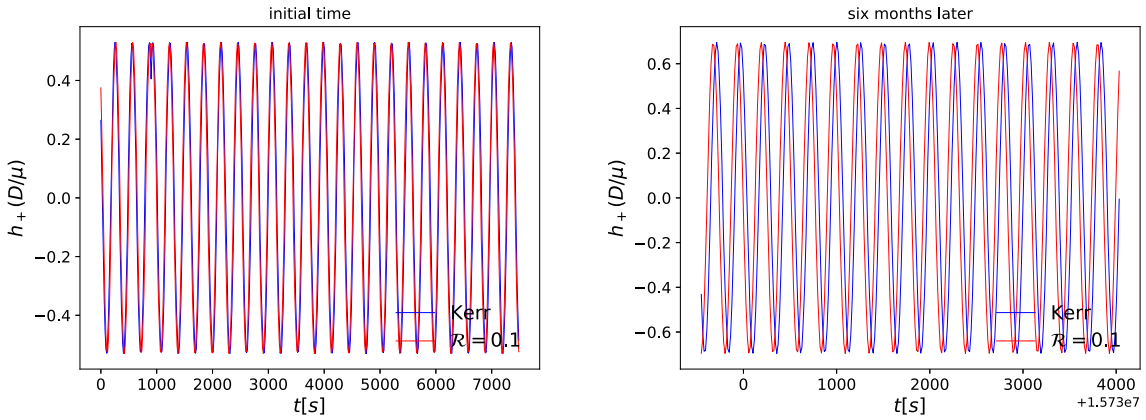

Fig. 3 Comparison between the polarizations h_+ of two kinds of waveform emitted from the spacetime of MHO and MBH for spin $a = 0.9$ of primary object is plotted, where the reflectivity and surface location of MHO is $\mathcal{R} = 10^{-2}$ and $x_0 = -40M$, respectively. The left panel of the above figure is the early stage of the full EMRI waveform and the right panel denotes to the last 4000 s, where the length of waveform is set as 1 year

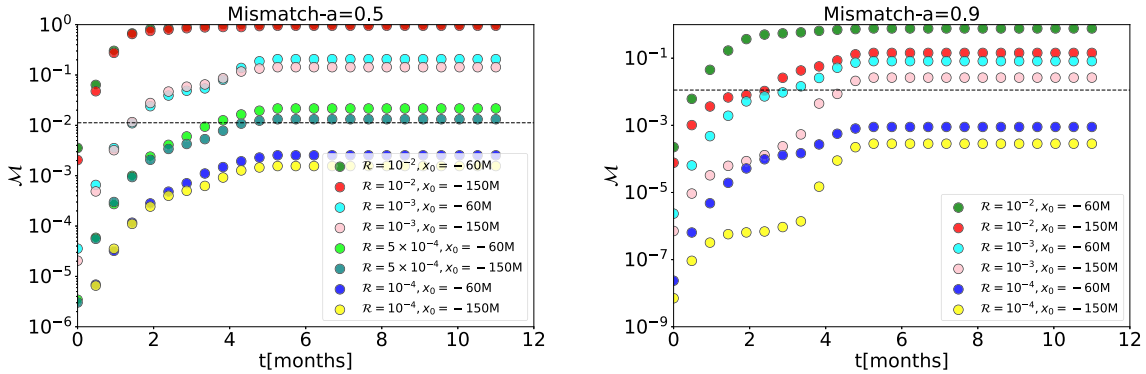

Fig. 4 Mismatch $\mathcal{M}$ as the function of observation time of EMRI is depicted for spin $a = 0.5$ (left panel) and $a = 0.9$ (right panel) respectively. These plots include several cases of reflectivities $\mathcal{R} = (10^{-2}, 10^{-3}, 5 \times 10^{-4}$ (left panel), $10^{-4})$,and locations $x_0 = (-60\,M, -150\,M)$

sic parameters of parameters describing the EMRI system [68,69].

From Fig. 4, the mismatch increases monotonically in observation time for LISA. As shown in the left panel of Fig. 4, the circular points above the horizontal dotted line denote sources can be distinguished by LISA for the case $a = 0.5$ of spinning MHO. From the figure, it is found that the threshold value of reflectivity and location are about $\mathcal{R} = 5 \times 10^{-4}$ and $x_0 = -150\,M$. Specifically, the EMRI source with reflectivity $\mathcal{R} = 5 \times 10^{-4}$ can be identified with the observation of five months. For MHO with reflectivity $\mathcal{R} = 10^{-3}$, the EMRI sources can be distinguished with two months observation for LISA. From the right panel of Fig. 4, for the case of high spinning MHO with $a = 0.9$, we plot the mismatch using waveform from EMRI systems with $\mathcal{R} = (10^{-2}, 10^{-3}, 5 \times 10^{-4}$ (left panel), $10^{-4})$ and locations $x_0 = (-60\,M, -150\,M)$. According to right panel, EMRI sources with locations $x_0 = -60M$ and reflectivity $\mathcal{R} = 10^{-3}$ can be discerned with five months observation of LISA, however, sources with locations $x_0 = -150M$ can not be distinguished. After the comparison of two panels in Fig. 4, for EMRI systems with the same reflectivities and locations, sources with lower spinning MBH can be distinguished by LISA. The conclusion is consistent with the trajectories results in Fig. 2.

These constraints on reflectivity are based on the suitable scenarios, in which the EMRI signal is modeled under the lower frequency approximate condition. The more rigorous constraint result would be obtained with GW response of time-delay interferometry and more accurate statistically method, such as the Bayesian Markov Chain Monte Carlo parameter estimation [70]. Additionally, in Ref. [25], an analytical model of gravitational-wave echoes in the post-merger signal of a binary coalescence was developed. The echoes signal is modified by the photon-sphere barrier, which is accompanied by the ringdown signal from a spinning ultracompact horizonless object. The time scale of echoes from the spinning remnants is less than that of EMRI, and their signaltonoise ratio (SNR) is smaller than that of EMRI signal from horizonless object. Therefore, the constraints of reflectivity

computed with the EMRI signal are more stringent than those with the echoes signal during the ringdown phase.

4 Conclusion

In this paper, we calculated the modified EMRI waveform, including the effect of horizonless object, by solving the Teukolsky equation with the artificial boundaries. The CO is assumed to be in motion on the circular and equatorial orbits near the MHO. The EMRI orbital dynamics are subjected to the boundaries at the reflective surface of MHO, leading to corrections in the GW energy flux and trajectory. With the procedures at hand, we have studies the difference in the GW trajectory and time domain waveform using frequency-independent reflectivity. We also have calculated the mismatch of EMRI waveforms from MBH and MHO to assess quantitatively the effect of horizonless object. Our results indicate that the observation of EMRI has the capacity to impose more rigorous restrictions on the reflectivity of MHO comparing to the echoes from post-merger phase of equivalent mass ratio binaries [25,71]. More specifically, LISA can distinguish between waveforms from MHO with the effective reflectivity as small as $\mathcal{R} \sim 5 \times 10^{-4}$ and waveforms from Kerr MBH.

In principle, MHOs with a reflective surface are predicted as alternatives to General Relativity (GR), including objects such as gavastars and boson stars [16,17,19]. Their optical appearances are similar to those of non-Kerr black holes, but their corresponding spacetime backgrounds are different. Therefore, the EMRI waveforms from the spacetimes of MHOs and non-Kerr black holes may exhibit deviations in waveform phases. To distinguish between EMRI waveforms of MHOs and non-Kerr black holes, it is necessary to accurately model the orbital dynamics and waveforms in two types of spacetimes. Future work should focus on the distinguishing the EMRI waveforms in the non-Kerr and MHO cases.

Although the reflectivity model we adopted is nonstandard, our current analysis and results about EMRI signal from MHO, to some extent, can characterize the main features of MHO. In the future work, we intent to explore a more physically meaningful model of reflectivity surface, which can be used to calculate echo waveforms for the general EMRI orbits. Additionally, it is crucial to develop reliable kludge EMRI waveform models that includes the effect of supermassive horizonless object. These models will be essential for performing data analyses of EMRI and parameter estimation using Bayesian method, as described in the relevant literatures [70,72].

Acknowledgements We are grateful to S. Hughes for the kind help about the calculation of the Teukolsky equation, thank Peng-Cheng Li and Jian-dong Zhang for reading the draft and providing helpful comments.

Funding T.G. Zi is funded by China Postdoctoral Science Foundation No. 2023M731137 and the National Natural Science Foundation of China (Grants No. 12347140).

Data Availability Statement This manuscript has no associated data. [Authors' comment: Data sharing not applicable to this article as no datasets were generated or analysed during the current study.]

Code Availability Statement The manuscript has no associated code/software. [Author's comment: Code/Software sharing not applicable to this article as no code/software was generated or analysed during the current study.]

Funded by SCOAP[3].

Appendix A: Transformations of SN equation and Teukolsky equation

In Sect. 2.2 we introduce briefly the asymptotic behaviors of Teukolsky and SN equations, and there exist some relations among these coefficients, which can be read with our symbol as following

$$
\begin{aligned}
{}_{\mathrm{SN}}B^{\mathrm{trans}} &= dB^{\mathrm{trans}}, && \text{(A1)}\\
{}_{\mathrm{SN}}B^{\mathrm{ref}} &= -4\omega^2 B^{\mathrm{ref}}, && \text{(A2)}\\
{}_{\mathrm{SN}}B^{\mathrm{inc}} &= -\frac{c_0}{4\omega} B^{\mathrm{inc}}, && \text{(A3)}\\
{}_{\mathrm{SN}}C^{\mathrm{trans}} &= -\frac{c_0}{4\omega} C^{\mathrm{trans}}, && \text{(A4)}\\
{}_{\mathrm{SN}}C^{\mathrm{ref}} &= dC^{\mathrm{ref}}, && \text{(A5)}\\
{}_{\mathrm{SN}}C^{\mathrm{inc}} &= gC^{\mathrm{inc}}, && \text{(A6)}
\end{aligned}
$$

where the aforementioned c_0, d and g are given by [55,73]

$$
\begin{aligned}
c_0 &= \lambda_{\ell m\omega}(2+\lambda_{\ell m\omega}) - 12\omega(a^2\omega + iM - am), && \text{(A7)}\\
d &= -2\sqrt{2Mr_+}\,(2am + i(r_- - r_+) - 4M\omega r_+)\\
&\quad \times (am + i(r_- - r+) - 2M\omega r_+) && \text{(A8)}\\
g &= \frac{b_0}{4\kappa(2Mr_+)^{3/2}(\kappa + 2i(r_+ - M)/(4Mr_+))}, && \text{(A9)}\\
b_0 &= \lambda_{\ell m\omega} + 2\lambda_{\ell m\omega} + 72\kappa M r_+\omega - 96\kappa^2 M^2\\
&\quad -12r_+^2\omega^2 - i(16\kappa M(\lambda_{\ell m\omega} + 3 - 3M/r_+)
\end{aligned}
$$

$$-12M\omega - 8\lambda_{\ell m\omega} r_+ \omega). \tag{A10}$$

Appendix B: Energy flux for Kerr BH

The energy flux from EMRI at infinity and near the horizon are given by [57,60,61]

$$\dot{E}^{\infty}_{\rm BH} = \sum_{\ell m} \frac{|Z^{\infty}_{\ell m\omega}|^2}{4\pi (m\Omega)^2}, \tag{B1}$$

$$\dot{E}^{H}_{\rm BH} = \sum_{\ell m} \frac{\alpha_{\ell m}|Z^{H}_{\ell m\omega}|^2}{4\pi (m\Omega)^2}, \tag{B2}$$

where

$$\alpha_{\ell m} = \frac{256(2Mr_+)^5 k(k^2+4\varpi^2)(k^2+16\varpi^2)(m\Omega)^3}{|c_{\ell m}|^2}, \tag{B3}$$

with $\varpi = \sqrt{M^2-a^2}/(4Mr_+)$ and

$$\begin{aligned} |c_{\ell m}|^2 &= ((\lambda+2)^2 + 4am\omega - 4(a\omega)^2)(\lambda^2 \\ &\quad +36am\omega - 36(a\omega)^2) \qquad \text{(B4)} \\ &\quad +(2\lambda+3)(96(a\omega)^2 - 48am\omega) \\ &\quad +144\omega^2(M^2-a^2), \qquad \text{(B5)} \end{aligned}$$

The gravitational amplitudes at infinity and near the horizon are the following

$$Z^{H}_{\ell m\omega} = C^{H}_{\ell m\omega} \int_{r_+}^{\infty} dr' \frac{\mathcal{T}_{\ell m\omega}(r') R^{\rm out}_{\ell m\omega}(r')}{\Delta^2(r')}, \tag{B6}$$

$$Z^{\infty}_{\ell m\omega} = C^{\infty}_{\ell m\omega} \int_{r_+}^{\infty} dr' \frac{\mathcal{T}_{\ell m\omega}(r') R^{\rm in}_{\ell m\omega}(r')}{\Delta^2(r')}, \tag{B7}$$

the source term $\mathcal{T}_{\ell m\omega}$ is given by [57,73]

$$\mathcal{T}_{lm\hat{\omega}} = 4\int d\hat{t} d\theta \sin\theta d\phi \frac{(B_2' + B_2'^{*})}{\bar{\rho}\rho^5} S_{lm\omega} e^{-i(m\phi+\hat{\omega}\hat{t})} \tag{B8}$$

where,

$$B_2' = -\frac{1}{2}\rho^8 \bar{\rho}\mathcal{L}_{-1}\left[\frac{1}{\rho^4}\mathcal{L}_0\left[\frac{T_{nn}}{\rho^2\bar{\rho}}\right]\right] \tag{B9}$$

$$-\frac{1}{2\sqrt{2}}\Delta^2\rho^8\bar{\rho}\mathcal{L}_{-1}\left[\frac{\bar{\rho}^2}{\rho^4}J_+\left[\frac{T_{\bar{m}n}}{\hat{\Delta}\rho^2\bar{\rho}^2}\right]\right], \tag{B10}$$

$$B_2'^{*} = -\frac{1}{4}\Delta^2\rho^8\bar{\rho}J_+\left[\frac{1}{\rho^4}J_+\left[\frac{\bar{\rho}}{\rho^2}T_{\bar{m}\bar{m}}\right]\right] \tag{B11}$$

$$-\frac{1}{2\sqrt{2}}\hat{\Delta}^2\rho^8\bar{\rho}J_+\left[\frac{\bar{\rho}^2}{\hat{\Delta}\rho^4}\mathcal{L}_{-1}\left[\frac{T_{\bar{m}n}}{\rho^2\bar{\rho}^2}\right]\right], \tag{B12}$$

the expression $\rho = 1/r^2$ and the operators are

$$\mathcal{L}_s = \frac{\partial}{\partial\theta} + \frac{m}{\sin\theta} - 2\cot\theta \quad ; \quad \mathcal{L}_s^{\dagger} = \frac{\partial}{\partial\theta} - \frac{m}{\sin\theta} - s\cot\theta. \tag{B13}$$

T_{nn}, $T_{\bar{m}n}$, and $T_{\bar{m}\bar{m}}$ are projections of the energy–momentum tensor with respect to Newman–Penrose tetrad, their full expression is found in Refs. [57,60,73]. Since the trajectories of point particle is the equatorial circular orbits, the equations (B6) is simplified as

$$Z^{\infty,H}_{\ell m\omega} = C^{\infty,H}_{\ell m\omega}\int_{r_+}^{\infty} dr'\left(A_0 - A_1\frac{d}{dr} + A_2\frac{d^2}{dr^2}\right)R^{\rm out,in}_{\ell m\omega}(r') \tag{B14}$$

where

$$A_0 = A_{nn0} + A_{\bar{m}n0} + A_{\bar{m}\bar{m}0}, \tag{B15}$$

$$A_1 = A_{\bar{m}n1} + A_{\bar{m}\bar{m}1}, \tag{B16}$$

$$A_2 = A_{\bar{m}\bar{m}2}, \tag{B17}$$

here the expressions A_{abi} with subscript $(ab = nn, \bar{m}n, \bar{m}\bar{m})$ and $i = 0, 1, 2$

$$A_{nn0} = -\frac{2C_{nn}}{\rho^3\rho^*\Delta^2}(\mathcal{L}_1^{\dagger}\mathcal{L}_2^{\dagger}S_{\ell m\omega} + 2i\rho\mathcal{L}_2^{\dagger}S_{\ell m\omega}), \tag{B18}$$

$$A_{\bar{m}n0} = -\frac{2\sqrt{2}C_{\bar{m}n}}{\rho^3\Delta}(iK/\Delta - \rho - \rho^*)\mathcal{L}_2^{\dagger}S_{\ell m\omega}, \tag{B19}$$

$$A_{\bar{m}\bar{m}0} = \frac{1}{\sqrt{2\pi}}S_{\ell m\omega}C_{\bar{m}\bar{m}}\rho^*/\rho^3[(K/\Delta)^2 - 2i\rho(K/\Delta) \tag{B20}$$

$$+id(K/\Delta)/dr], \tag{B21}$$

$$A_{\bar{m}n1} = \frac{2}{\sqrt{\pi}}\mathcal{L}_2^{\dagger}S_{\ell m\omega}C_{\bar{m}n}/(\rho^3\Delta), \tag{B22}$$

$$A_{\bar{m}\bar{m}1} = -\frac{2}{\sqrt{2\pi}}C_{\bar{m}\bar{m}}S_{\ell m\omega}(iK/\Delta + \rho)\rho^*/\rho^3, \tag{B23}$$

$$A_{\bar{m}\bar{m}2} = -\frac{1}{\sqrt{2\pi}}C_{\bar{m}\bar{m}}S_{\ell m\omega}\rho^*/\rho^3 \tag{B24}$$

where the full expressions of C_{ab} are found in Refs. [57,60,73], they can be written as

$$C_{nn} = \frac{1}{4\Sigma dt/d\tau}\left[E(r^2+a^2) - aL_z + \Sigma\frac{dr}{d\tau}\right], \tag{B25}$$

$$C_{\bar{m}\bar{m}} = \frac{\rho^2}{2\Sigma dt/d\tau}\left[i(aE - L_z) + \Sigma\frac{d\theta}{d\tau}\right], \tag{B26}$$

$$\begin{aligned} C_{\bar{m}n} &= -\frac{\rho}{2\sqrt{2}\Sigma dt/d\tau}\left[E(r^2+a^2) - aL_z + \Sigma\frac{dr}{d\tau}\right] \\ &\quad \times\left[i(aE - L_z) + \Sigma\frac{d\theta}{d\tau}\right] \qquad \text{(B27)} \end{aligned}$$

with the geodesic equations for the circular orbits on the equatorial plane of Kerr BH

$$\Sigma\frac{d\theta}{d\tau} = 0, \tag{B28}$$

$$\Sigma\frac{dr}{d\tau} = 0, \tag{B29}$$

$$\Sigma\frac{d\phi}{d\tau} = -(aE - Lz) + \frac{a}{\Delta}(E(r^2+a^2) - aL_z), \tag{B30}$$

$$\Sigma \frac{dt}{d\tau} = -a(aE - Lz) + \frac{r^2+a^2}{\Delta}(E(r^2+a^2) - aL_z). \tag{B31}$$

References

1. B.P. Abbott et al., (LIGO Scientific, Virgo), Phys. Rev. Lett. **116**, 061102 (2016). https://doi.org/10.1103/PhysRevLett.116.061102. arXiv:1602.03837 [gr-qc]
2. B.P. Abbott et al., (LIGO Scientific, Virgo), Phys. Rev. X **9**, 031040 (2019). https://doi.org/10.1103/PhysRevX.9.031040. arXiv:1811.12907 [astro-ph.HE]
3. B.P. Abbott et al., (LIGO Scientific, Virgo), Phys. Rev. Lett. **116**, 241103 (2016). https://doi.org/10.1103/PhysRevLett.116.241103. arXiv:1606.04855 [gr-qc]
4. B.P. Abbott et al., (LIGO Scientific, Virgo), Ann. Phys. **529**, 1600209 (2017). https://doi.org/10.1002/andp.201600209. arXiv:1608.01940 [gr-qc]
5. B.P. Abbott et al., (LIGO Scientific, VIRGO), Phys. Rev. Lett. **118**, 221101 (2017) (Erratum: Phys. Rev. Lett. 121, 129901 (2018)). https://doi.org/10.1103/PhysRevLett.118.221101. arXiv:1706.01812 [gr-qc]
6. J. Abadie et al., (LIGO Scientific), Nat. Phys. **7**, 962 (2011). https://doi.org/10.1038/nphys2083. arXiv:1109.2295 [quant-ph]
7. P. Amaro-Seoane et al., (LISA), (2017). arXiv:1702.00786 [astro-ph.IM]
8. J. Luo et al., (TianQin), Class. Quantum Gravity **33**, 035010 (2016). https://doi.org/10.1088/0264-9381/33/3/035010. arXiv:1512.02076 [astro-ph.IM]
9. W.-H. Ruan, Z.-K. Guo, R.-G. Cai, Y.-Z. Zhang, Int. J. Mod. Phys. A **35**, 2050075 (2020). https://doi.org/10.1142/S0217751X2050075X. arXiv:1807.09495 [gr-qc]
10. V. Cardoso, P. Pani, Living Rev. Relativ. **22**, 4 (2019). https://doi.org/10.1007/s41114-019-0020-4. arXiv:1904.05363 [gr-qc]
11. E. Berti et al., Class. Quantum Gravity **32**, 243001 (2015). https://doi.org/10.1088/0264-9381/32/24/243001. arXiv:1501.07274 [gr-qc]
12. B.P. Abbott et al. (LIGO Scientific, Virgo), Phys. Rev. Lett. **116**, 221101 (2016) (Erratum: Phys. Rev. Lett. 121, 129902 (2018)). https://doi.org/10.1103/PhysRevLett.116.221101. arXiv:1602.03841 [gr-qc]
13. V. Cardoso, L. Gualtieri, Class. Quantum Gravity **33**, 174001 (2016). https://doi.org/10.1088/0264-9381/33/17/174001. arXiv:1607.03133 [gr-qc]
14. S. Babak, J. Gair, A. Sesana, E. Barausse, C.F. Sopuerta, C.P.L. Berry, E. Berti, P. Amaro-Seoane, A. Petiteau, A. Klein, Phys. Rev. D **95**, 103012 (2017). https://doi.org/10.1103/PhysRevD.95.103012. arXiv:1703.09722 [gr-qc]
15. T.-G. Zi, J.-D. Zhang, H.-M. Fan, X.-T. Zhang, Y.-M. Hu, C. Shi, J. Mei, Phys. Rev. D **104**, 064008 (2021). https://doi.org/10.1103/PhysRevD.104.064008. arXiv:2104.06047 [gr-qc]
16. P.O. Mazur, E. Mottola, (2001). arXiv:gr-qc/0109035
17. P.O. Mazur, E. Mottola, Proc. Nat. Acad. Sci. **101**, 9545 (2004). https://doi.org/10.1073/pnas.0402717101. arXiv:gr-qc/0407075
18. S.D. Mathur, Fortsch. Phys. **53**, 793 (2005). https://doi.org/10.1002/prop.200410203. arXiv:hep-th/0502050
19. D. Guerra, C.F.B. Macedo, P. Pani, JCAP **09**, 061 (2019) (Erratum: JCAP 06, E01 (2020)). https://doi.org/10.1088/1475-7516/2019/09/061. arXiv:1909.05515 [gr-qc]
20. A. Almheiri, D. Marolf, J. Polchinski, J. Sully, JHEP **02**, 062 (2013). https://doi.org/10.1007/JHEP02(2013)062. arXiv:1207.3123 [hep-th]
21. M.S. Morris, K.S. Thorne, U. Yurtsever, Phys. Rev. Lett. **61**, 1446 (1988). https://doi.org/10.1103/PhysRevLett.61.1446
22. B. Holdom, J. Ren, Phys. Rev. D **95**, 084034 (2017). https://doi.org/10.1103/PhysRevD.95.084034. arXiv:1612.04889 [gr-qc]
23. E. Maggio, L. Buoninfante, A. Mazumdar, P. Pani, Phys. Rev. D **102**, 064053 (2020). https://doi.org/10.1103/PhysRevD.102.064053. arXiv:2006.14628 [gr-qc]
24. V. Cardoso, E. Franzin, P. Pani, Phys. Rev. Lett. **116**, 171101 (2016) (Erratum: Phys. Rev. Lett. 117, 089902 (2016)). https://doi.org/10.1103/PhysRevLett.116.171101. arXiv:1602.07309 [gr-qc]
25. E. Maggio, A. Testa, S. Bhagwat, P. Pani, Phys. Rev. D **100**, 064056 (2019). https://doi.org/10.1103/PhysRevD.100.064056. arXiv:1907.03091 [gr-qc]
26. N. Oshita, N. Afshordi, Phys. Rev. D **99**, 044002 (2019). https://doi.org/10.1103/PhysRevD.99.044002. arXiv:1807.10287 [gr-qc]
27. J. Abedi, H. Dykaar, N. Afshordi, Phys. Rev. D **96**, 082004 (2017). https://doi.org/10.1103/PhysRevD.96.082004. arXiv:1612.00266 [gr-qc]
28. Q. Wang, N. Oshita, N. Afshordi, Phys. Rev. D **101**, 024031 (2020). https://doi.org/10.1103/PhysRevD.101.024031. arXiv:1905.00446 [gr-qc]
29. V. Cardoso, P. Pani, Nat. Astron. **1**, 586 (2017). https://doi.org/10.1038/s41550-017-0225-y. arXiv:1709.01525 [gr-qc]
30. R.S. Conklin, B. Holdom, J. Ren, Phys. Rev. D **98**, 044021 (2018). https://doi.org/10.1103/PhysRevD.98.044021. arXiv:1712.06517 [gr-qc]
31. V. Cardoso, S. Hopper, C.F.B. Macedo, C. Palenzuela, P. Pani, Phys. Rev. D **94**, 084031 (2016). https://doi.org/10.1103/PhysRevD.94.084031. arXiv:1608.08637 [gr-qc]
32. J. Abedi (2022). arXiv:2301.00025 [gr-qc]
33. E. Berti et al., (2019). arXiv:1903.02781 [astro-ph.HE]
34. C.P.L. Berry, S.A. Hughes, C.F. Sopuerta, A.J.K. Chua, A. Heffernan, K. Holley-Bockelmann, D.P. Mihaylov, M.C. Miller, A. Sesana (2019). arXiv:1903.03686 [astro-ph.HE]
35. K.G. Arun et al., (LISA), Living Rev. Relativ. **25**, 4 (2022). https://doi.org/10.1007/s41114-022-00036-9. arXiv:2205.01597 [gr-qc]
36. A. Pound, Fund. Theor. Phys. **179**, 399 (2015). https://doi.org/10.1007/978-3-319-18335-0_13. arXiv:1506.06245 [gr-qc]
37. L. Barack, A. Pound, Rep. Prog. Phys. **82**, 016904 (2019). https://doi.org/10.1088/1361-6633/aae552. arXiv:1805.10385 [gr-qc]
38. S. Datta, Phys. Rev. D **102**, 064040 (2020). https://doi.org/10.1103/PhysRevD.102.064040. arXiv:2002.04480 [gr-qc]
39. S. Datta, R. Brito, S. Bose, P. Pani, S.A. Hughes, Phys. Rev. D **101**, 044004 (2020). https://doi.org/10.1103/PhysRevD.101.044004. arXiv:1910.07841 [gr-qc]
40. S. Datta, S. Bose, Phys. Rev. D **99**, 084001 (2019). https://doi.org/10.1103/PhysRevD.99.084001. arXiv:1902.01723 [gr-qc]
41. P. Pani, A. Maselli, Int. J. Mod. Phys. D **28**, 1944001 (2019). https://doi.org/10.1142/S0218271819440012. arXiv:1905.03947 [gr-qc]
42. G.A. Piovano, A. Maselli, P. Pani, Phys. Rev. D **107**, 024021 (2023). https://doi.org/10.1103/PhysRevD.107.024021. arXiv:2207.07452 [gr-qc]
43. E. Maggio, M. van de Meent, P. Pani, Phys. Rev. D **104**, 104026 (2021). https://doi.org/10.1103/PhysRevD.104.104026. arXiv:2106.07195 [gr-qc]
44. N. Sago, T. Tanaka, Phys. Rev. D **104**, 064009 (2021). https://doi.org/10.1103/PhysRevD.104.064009. arXiv:2106.07123 [gr-qc]
45. I. Agullo, V. Cardoso, A.D. Rio, M. Maggiore, J. Pullin, Phys. Rev. Lett. **126**, 041302 (2021). https://doi.org/10.1103/PhysRevLett.126.041302. arXiv:2007.13761 [gr-qc]
46. S. Datta, K.S. Phukon, Phys. Rev. D **104**, 124062 (2021). https://doi.org/10.1103/PhysRevD.104.124062. arXiv:2105.11140 [gr-qc]
47. E. Maggio, P. Pani, V. Ferrari, Phys. Rev. D **96**, 104047 (2017). https://doi.org/10.1103/PhysRevD.96.104047. arXiv:1703.03696 [gr-qc]

48. Z. Mark, A. Zimmerman, S.M. Du, Y. Chen, Phys. Rev. D **96**, 084002 (2017). https://doi.org/10.1103/PhysRevD.96.084002. arXiv:1706.06155 [gr-qc]
49. A. Maselli, N. Franchini, L. Gualtieri, T.P. Sotiriou, Phys. Rev. Lett. **125**, 141101 (2020). https://doi.org/10.1103/PhysRevLett.125.141101. arXiv:2004.11895 [gr-qc]
50. G. Raposo, P. Pani, R. Emparan, Phys. Rev. D **99**, 104050 (2019). https://doi.org/10.1103/PhysRevD.99.104050. arXiv:1812.07615 [gr-qc]
51. J.M. Bardeen, W.H. Press, S.A. Teukolsky, Astrophys. J. **178**, 347 (1972). https://doi.org/10.1086/151796
52. S.A. Teukolsky, Phys. Rev. Lett. **29**, 1114 (1972). https://doi.org/10.1103/PhysRevLett.29.1114
53. S.A. Teukolsky, *Perturbations of a rotating black hole*, Ph.D. thesis, Caltech (1973)
54. Black Hole Perturbation Toolkit. http://bhptoolkit.org/bhptoolkit.org
55. M. Sasaki, T. Nakamura, Prog. Theor. Phys. **67**, 1788 (1982). https://doi.org/10.1143/PTP.67.1788
56. M. Sasaki, T. Nakamura, Phys. Lett. A **89**, 68 (1982). https://doi.org/10.1016/0375-9601(82)90507-2
57. S.A. Teukolsky, W.H. Press, Astrophys. J. **193**, 443 (1974). https://doi.org/10.1086/153180
58. H. Nakano, N. Sago, H. Tagoshi, T. Tanaka, PTEP **2017**, 071E01 (2017). https://doi.org/10.1093/ptep/ptx093. arXiv:1704.07175 [gr-qc]
59. L.F. Longo Micchi, N. Afshordi, C. Chirenti, Phys. Rev. D **103**, 044028 (2021). https://doi.org/10.1103/PhysRevD.103.044028. arXiv:2010.14578 [gr-qc]
60. S.A. Hughes, Phys. Rev. D **61**, 084004 (2000) (Erratum: Phys. Rev. D 63, 049902 (2001), Erratum: Phys. Rev. D 65, 069902 (2002), Erratum: Phys. Rev. D 67, 089901 (2003), Erratum: Phys. Rev. D 78, 109902 (2008), Erratum: Phys. Rev. D 90, 109904 (2014)). https://doi.org/10.1103/PhysRevD.65.069902. arXiv:gr-qc/9910091
61. S.A. Hughes, Phys. Rev. D **64**, 064004 (2001) (Erratum: Phys. Rev. D 88, 109902 (2013)). https://doi.org/10.1103/PhysRevD.64.064004. arXiv:gr-qc/0104041
62. S.A. Hughes, N. Warburton, G. Khanna, A.J.K. Chua, M.L. Katz, Phys. Rev. D **103**, 104014 (2021). https://doi.org/10.1103/PhysRevD.103.104014. arXiv:2102.02713 [gr-qc]
63. T. Hinderer, E.E. Flanagan, Phys. Rev. D **78**, 064028 (2008). https://doi.org/10.1103/PhysRevD.78.064028. arXiv:0805.3337 [gr-qc]
64. S. Mano, H. Suzuki, E. Takasugi, Prog. Theor. Phys. **95**, 1079 (1996). https://doi.org/10.1143/PTP.95.1079. arXiv:gr-qc/9603020
65. R. Fujita, H. Tagoshi, Prog. Theor. Phys. **112**, 415 (2004). https://doi.org/10.1143/PTP.112.415. arXiv:gr-qc/0410018
66. R. Fujita, W. Hikida, H. Tagoshi, Prog. Theor. Phys. **121**, 843 (2009). https://doi.org/10.1143/PTP.121.843. arXiv:0904.3810 [gr-qc]
67. C. Cutler, Phys. Rev. D **57**, 7089 (1998). https://doi.org/10.1103/PhysRevD.57.7089
68. E.E. Flanagan, S.A. Hughes, Phys. Rev. D **57**, 4566 (1998). https://doi.org/10.1103/PhysRevD.57.4566. arXiv:gr-qc/9710129
69. L. Lindblom, B.J. Owen, D.A. Brown, Phys. Rev. D **78**, 124020 (2008). https://doi.org/10.1103/PhysRevD.78.124020. arXiv:0809.3844 [gr-qc]
70. M.L. Katz, A.J.K. Chua, L. Speri, N. Warburton, S.A. Hughes, Phys. Rev. D **104**, 064047 (2021). https://doi.org/10.1103/PhysRevD.104.064047. arXiv:2104.04582 [gr-qc]
71. A. Testa, P. Pani, Phys. Rev. D **98**, 044018 (2018). https://doi.org/10.1103/PhysRevD.98.044018. arXiv:1806.04253 [gr-qc]
72. A.J.K. Chua, N. Korsakova, C.J. Moore, J.R. Gair, S. Babak, Phys. Rev. D **101**, 044027 (2020). https://doi.org/10.1103/PhysRevD.101.044027. arXiv:1912.11543 [astro-ph.IM]
73. M. Sasaki, H. Tagoshi, Living Rev. Relativ. **6**, 6 (2003). https://doi.org/10.12942/lrr-2003-6. arXiv:gr-qc/0306120